Proceedings World Geothermal Congress 2020+1
Reykjavik, Iceland, April - October 2021

Microearthquake Monitoring at Salak Geothermal Field, Indonesia: Application of Tomography Inversion and Its Impact on Reservoir Characterization

Muhamad Wildan Perdana[1], Denny Mendrofa[1], Taufiq Lubis[1], Gregg Nordquist[2]

Star Energy Geothermal Salak[1]

Independent Consultant[2]

Star Energy Geothermal, Sentral Senayan II Office Tower, 26th Fl., Jakarta, Indonesia

wildan.perdana@starenergy.co.id

Keywords: Salak, microearthquake, tomography, velocity model

ABSTRACT

Continuous microearthquake (MEQ) monitoring has been conducted since 1995 at Salak geothermal field. During 1995 to 2005, a five-station telemetered analog monitoring array was deployed. Since 2005, MEQ monitoring has been performed using a network of 10-13 portable 24-bit digital stations. So far, more than 12,000 MEQ events have been recorded at Salak field. Analyses show that microseismicity is induced by injection and production activities, and during stimulation of wells. Until 2016, in-house MEQ processing and analysis were limited to event determination and correlation with field activities. More advanced MEQ processing was implemented in 2016, which includes velocity tomography inversion to provide models for the compressional (Vp) and shear wave (Vs) velocity structures. In 2018, two new velocity models were developed: an updated 1D and a new 3D model. The relocated MEQs using the new 3D velocity model showed very little change in the epicenters, but fieldwide, the hypocenters tend to deepen and show a tighter clustering.

Initial results of the MEQ 3D tomography study at Salak field show this method's potential to provide valuable information for reservoir characterization. Current results of the tomographic modeling define systematic lateral and vertical changes of the Salak geothermal reservoir's velocity structure. This includes a lower Vp centered over the productive field. Preliminary cross-plot analysis of Vp with pressure, matrix porosity, and fracture permeability suggest these may play a role in the Vp distribution across the field. Further analysis is underway to understand the link between Vp, Vs, and Vp/Vs with other reservoir parameters. Insight from these studies are being used to provide a better conceptual understanding of the Salak reservoir. This includes a mapping of the depth extent of the stimulated connected fracture network (Base of Reservoir) used in the dynamic numerical simulation model.

1. INTRODUCTION

Star Energy Geothermal (SEG) operates Salak (Awibengkok) geothermal field located in West Java province, Indonesia, which is about 70 km south of Jakarta (Figure 1). The original exploration contract area, including the current proven field lies in a highland on the southwestern flank of the Gunung Salak volcano, for which the contract area was named (Stimac, 2008). First commissioning of electricity generation was in 1994 with two 55 MWe power plants installed. Production was increased to a nominal capacity of 330 MWe in late 1997 (Soeparjadi et al., 1998) by expanding production to the eastern portion of the proven reservoir. In 1997–1999, the operating contract with the Government of Indonesia called for increased production from Awibengkok. As a result, the field has operated at 377 MWe since late 2002 (Acuna et al., 2008).

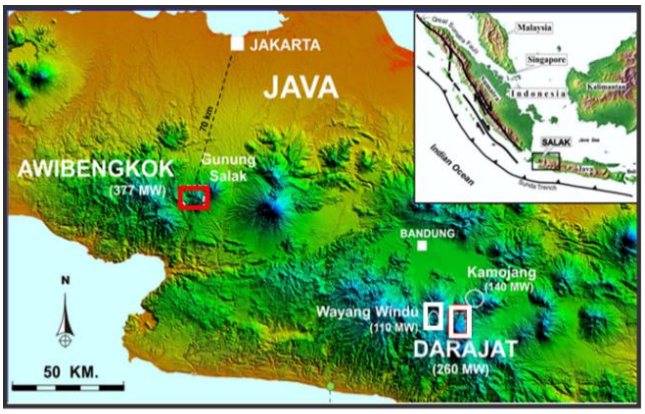

Source: SRTM West Java BSL 1841_Z48S

Figure 1: Location of the Salak (Awibengkok) geothermal field in West Java province, Indonesia. The two white rectangles show the location of the other geothermal fields operated by SEG.

At Salak, SEG has conducted continuous microseismic or microearthquake (MEQ) monitoring since 1995. The initial array consisted of five analog instruments that were telemetered to a central computer for processing and analysis. Starting in 2005, MEQ monitoring was upgraded to implement a portable digital array using 24-bit SMART-24R (Geotech, Ltd.) instruments and three-component

4.5 Hz seismometer that are buried at approximately a meter depth. The currently deployed microseismic monitoring array consists of from 10-13 instruments distributed around the field (Figure 2). This provides monitoring coverage of the main Salak field (production and injection) and the Cianten Caldera (injection).

During processing, data were uploaded weekly from the field instruments, time-associated, and ran through an auto picker. These MEQ events were individually checked and the P- and S-wave arrival times for the local events were handpicked (Nelson, 2018). For the initial interpretation and analysis, the events were located using a 1D model, using the Seisplus software paired with Geotech, Ltd. instruments. Until recently, SEG's analysis of the extensive database of MEQ events (>12,000) was limited to single event locations using a 1D velocity model and correlation with field with injection and production activities. This paper outlines the results from implementation of a new analysis package and the workflows that SEG developed to create and interpret 3D tomographic velocity models.

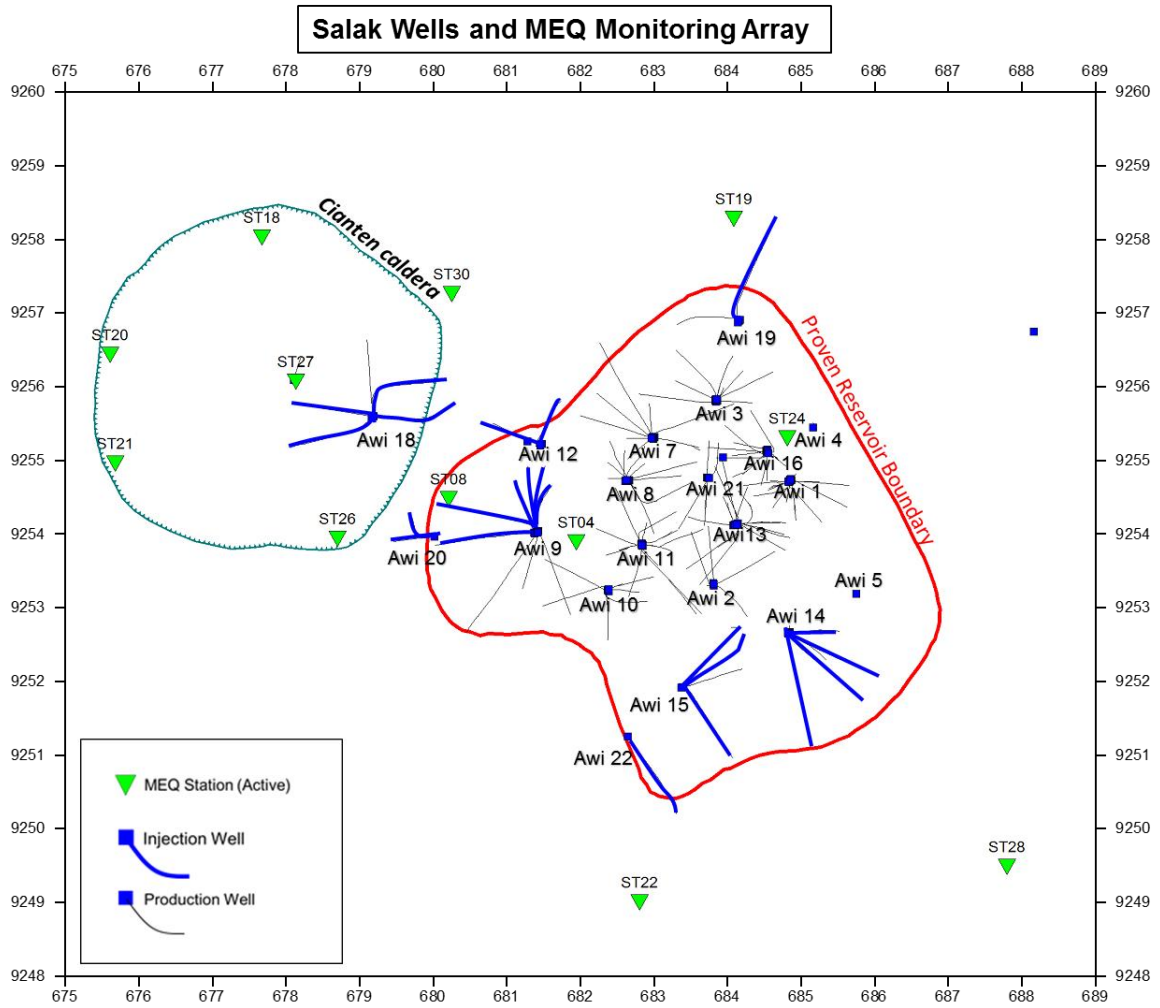

Figure 2: Location of Salak production and injection wells and MEQ network array distributed around Salak geothermal field.

2. INDUCED MICROSEISMICITY

An MEQ event is typically defined as earthquake that has magnitude below M 3. MEQs with this magnitude cannot normally be felt and do not result in damage at the surface, the local community or the geothermal fields' infrastructure. MEQs can be triggered when fluids are injected into highly-stressed rock. Seismicity triggered by fluid injection tends to be distributed throughout a small volume with fairly well-defined limits (Gibson and Sandiford, 2013). In geothermal operations, the presence of MEQs can be induced by injection and production activities.

In Salak, the continuous MEQ monitoring conducted since 1995 defines distinct clusters of induced microseismicity that are associated with injection, production, and stimulation of wells. The distribution of MEQ epicenters have general SW–NE and WSW–NNE orientations, which are parallel to the major trend of structures observed through the Salak field. Figure 3 shows the fieldwide MEQ occurrence in Salak during 2005 to 2018: about 12,000 events have been recorded during this period.

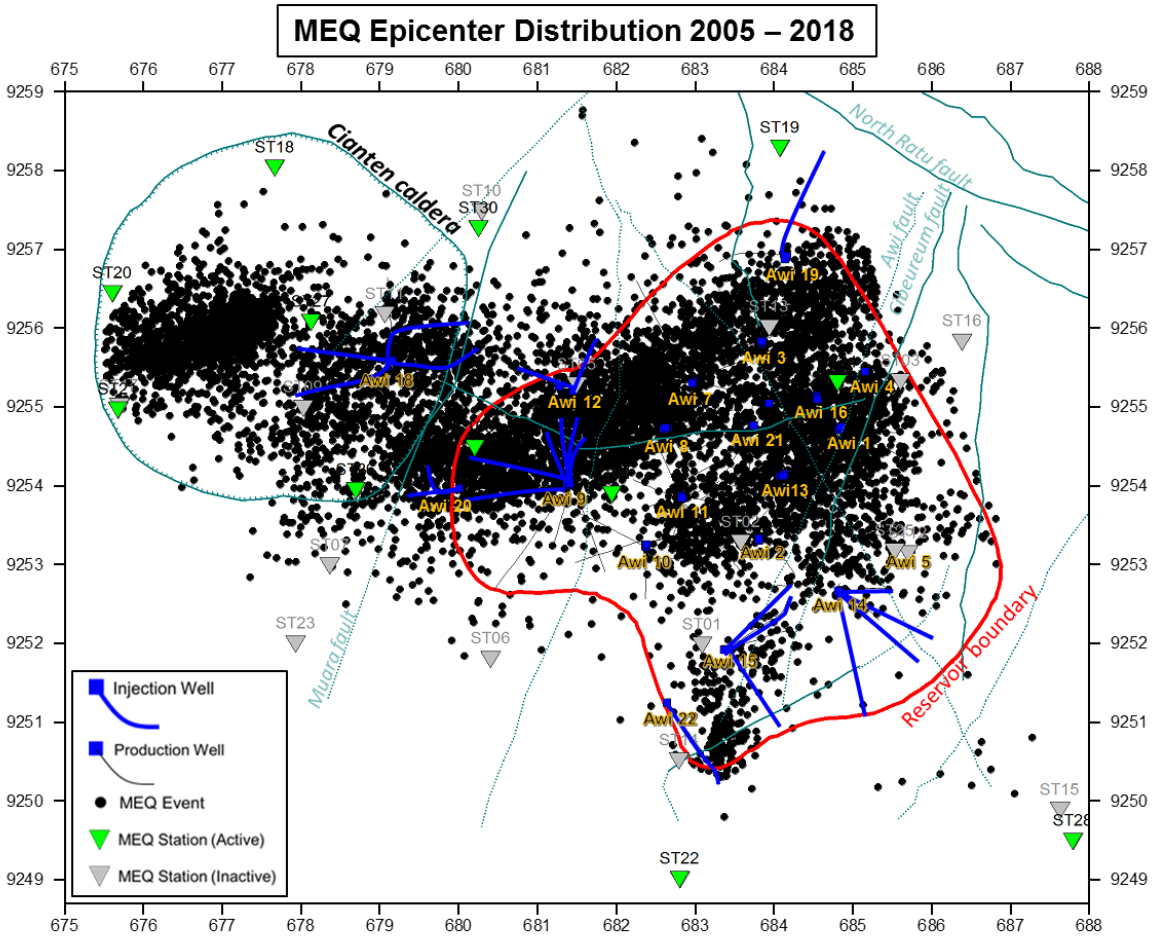

Figure 3: MEQ epicenter distribution in Salak field during 2005 to 2018. MEQs are clustered distinctively and associated with specific triggering mechanism: injection, production, and stimulation of wells.

The majority of MEQ occurrence in Salak is related to injection activity. This was interpreted based on the strong spatial and temporal correlations of the MEQs and their distribution with both brine and condensate injection, which are located near the field margins and outside the reservoir. The induction mechanism of these injection-related MEQ is interpreted to be related with injection pressure or temperature transients in the pre-existing fracture system. Mossop and Segall (2004) discussed in detail these two mechanisms and their implication in interpreting MEQ activity. It is believed that the dominant mechanism of injection-induced microearthquakes in Salak is probably related to pressure perturbations, and both pressure and temperature transients probably play a role in their occurrence. MEQs occur within a fracture network stressed near to failure. Stresses are likely to build up in areas of the natural fracture network with relatively low permeability or along major tectonic structures (Nordquist, 1998). In many cases, MEQ occurrence frequency has a strong temporal correspondence with injection activity. This is most evident during the startup of injection in a new well, or when injection rates are changed. However, there are also many cases where MEQ clusters are observed near injectors that but are not associated with abrupt changes of injection rates. For these cases, it is interpreted the MEQs result following a build-up of pressure in the fracture network related to the injection releasing energy when the fracture network reaches a critical stress in the Mohr failure envelope (Perdana, 2018).

The second most common cause microseismicity occurrence is due to production activity. For instance, several MEQ clusters can be found in the central of the production area where no injection takes place (Figure 4). Interestingly, the MEQ activity in the production area did not start until about 2002. By 2004, an obvious clustering in the steam cap area presumably related to production activity started to occur, about nearly 10 years after production was started in the field. Thus, the occurrence of MEQ clusters in the vicinity of production area is interpreted mainly to be caused by the mass extraction in the steam cap, which creates pressure drops in the pores and fractures system. The lack of pressure support then results in reservoir compaction. This compaction might induce stress release inside the area and correspond to microseismic activity (Nelson, 2012). Other prominent MEQ occurrence in Salak is the distinct areal MEQ hypocenter trend between the west and east portions of the field. In the west, MEQs tend to be distributed deeper compared to what is shown in eastern area. The deep MEQs in the west are mainly related to brine injection from the Awi 9 pad that has been operating since initial production in 1994 and later (2008) condensate injection in Awi 18 and Awi 20 pads. The hypocenter of MEQs in the west portion of Salak are located about 500 m BSL (meters Below Sea Level) to 4,500 m BSL. In the east, MEQs that are related to production and also injection activities have generally shallower depth range of about 500 m ASL (meters Above Sea Level) to 1,000 m BSL (Figure 4).

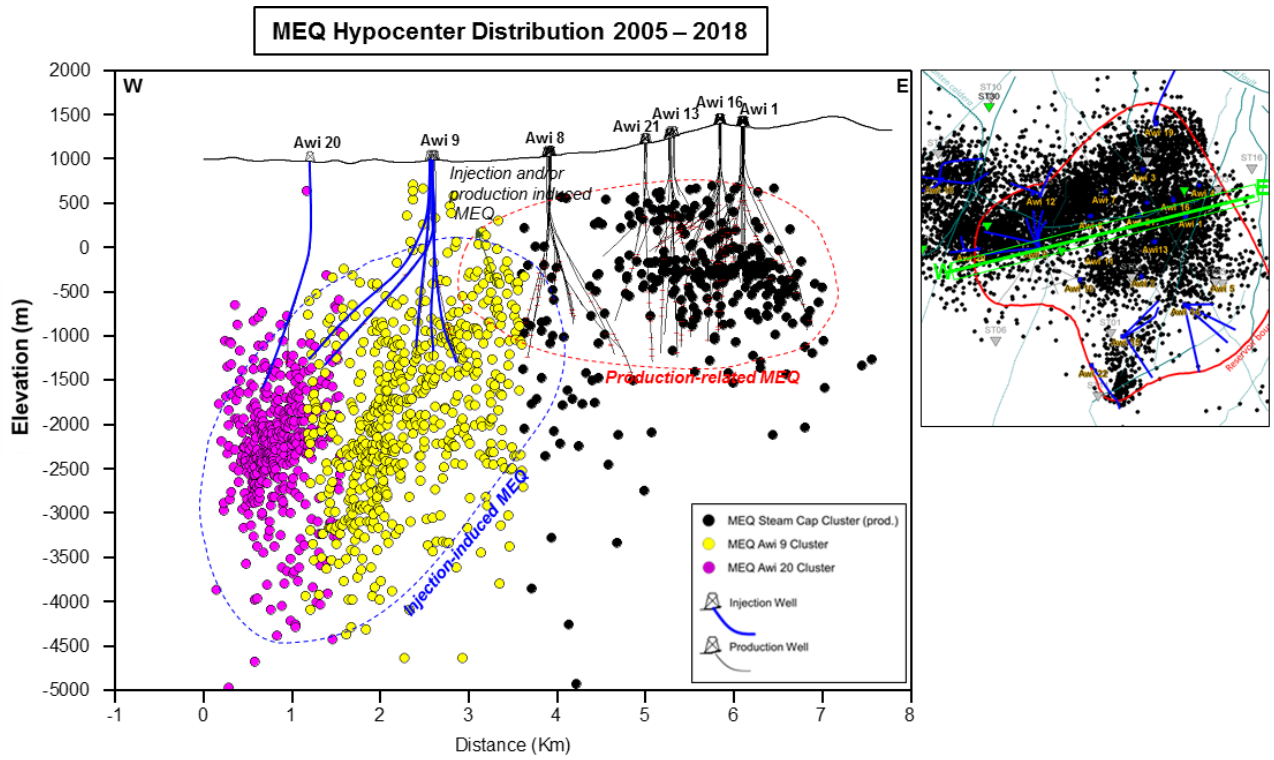

Figure 4: W-E cross section showing MEQ hypocenter distribution during 2005 to 2018. The west portion of the MEQ cluster, is mainly related to injection, is generally deeper compared to the MEQs in the east portion, which are injection- and production-related).

Induced MEQ activity also has a clear correlation with injection stimulation as shown by MEQ occurrence during the early stage of stimulation of Awi 18-1. In 2008, Salak field started to utilize Awi 18-1 as an outfield condensate injector in the Cianten Caldera located west of the proven commercial reservoir boundary. Prior to starting injection stimulation, there were no MEQs located near Awi 18-1. Stimulation of Awi 18-1 was conducted in two phases with the first phase during May 8 to August 22, 2007 (Figure 5a). For the 1st phase, the average Injection Wellhead Pressure (IWHP) was 345 psia and injection rate was about 63 kph; during this phase, MEQs occurred near the TD of Awi 18-1 but only small number of events (Figure 5b). Daily average of MEQ occurrence is only about 0.2 event/day with a maximum of two MEQ in a single day. The 2nd phase began on October 31, 2007 until August 26, 2008. Additional pumps were added so that the injection rate and IWHP could be increased. A total of 7,909,532 barrels of condensate, representing about 97% of the total condensate injected during the whole stimulation, was injected during this second phase of stimulation. The average IWHP during this phase was 468 psia with a maximum of 888 psia. Average rate of injected condensate was about 440 kph with a maximum rate of 746 kph. During the 2nd period of stimulation with higher IWHP and injection rates, there was noticeable increase of MEQ occurrence to 0.8 event/day with a maximum of 15 events recorded in a single day. This MEQ occurrence rate is more than twice compared to the first injection stimulation period. MEQs extended vertically to an elevation of about 5,000 m BSL indicating structures with steep to almost vertical dip and delineated the pathway of injectate movement (Wibowo, 2010). Since the stimulation of Awi 18-1, three more wells have been drilled in the Awi 18 pad. Injection and stimulation of these new wells resulted in the occurrence of MEQ clusters south and west of the Awi 18 wells providing important insights into the extent of the stimulated fracture network in the Cianten Caldera (Tanuwidjaja et al., 2015).

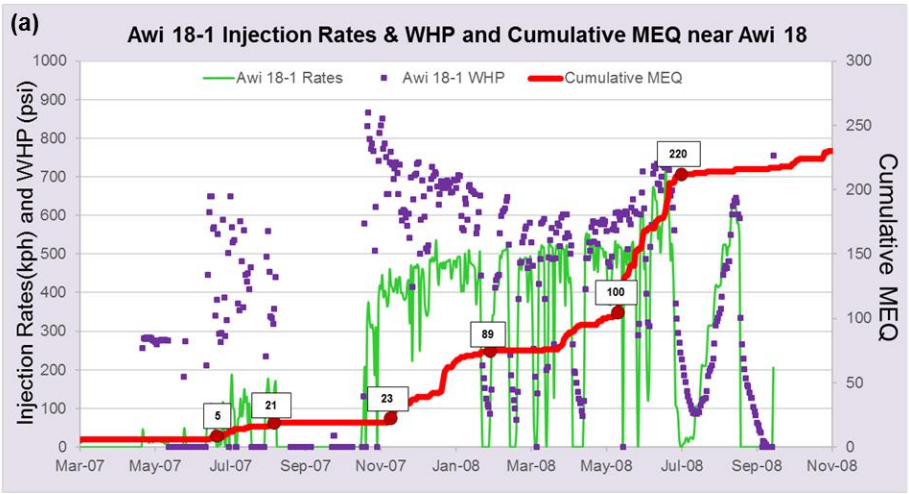

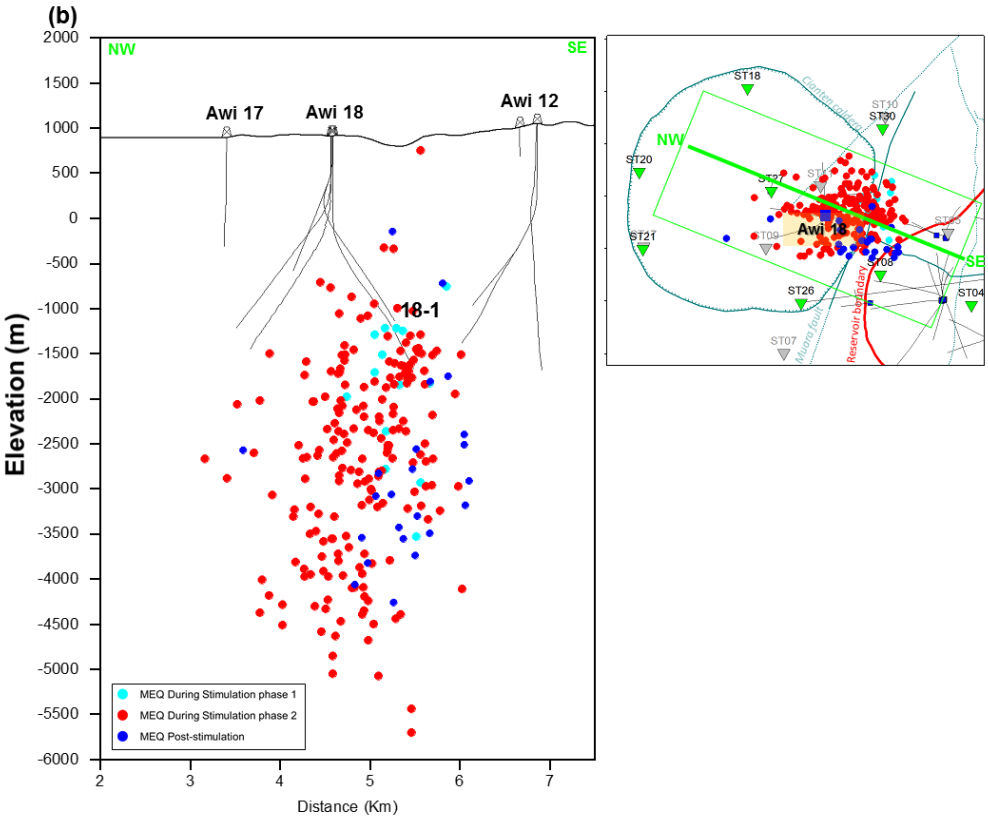

Figure 5: (a) Awi 18-1 injection stimulation rates (purple squares), IWHP (green curve), and cumulative MEQ (red curve) in the vicinity of Awi 18-1 during this well's injection stimulation. Note the few MEQs at lower average injection rate (63 kph) and IWHP (467.5 psia) and significant number of MEQs at higher injection rate and IWHP. (b) Cross-section showing MEQ hypocenter distribution during the 1st, 2nd and post-stimulation stages. In general, MEQs occur just below to as deep as 5,000 m BSL during the injection stimulation of AWI 18-1 indicating the extent of the fracture network.

3. TOMOGRAPHY INVERSION

Tomography is a primary method for the estimation of seismic velocity variations (Biasi et al., 2009). In this study, SEG utilized the software package Microseisgram/JTOMO (Altcom, Ltd.). This package provides a powerful "toolbox" for the QC and processing of MEQ data.

SEG's workflow for the tomographic inversion is summarized in Figure 6. In this workflow, a 1D (horizontally-layered) model is developed first using the initial MEQ locations and a half-space starting model. The results from the first inversion is utilized as the starting velocity for the following inversions and so on. The inversion is finalized when a stable result for the Vp and Vs is obtained for the 1D model (Nelson, 2018). This new 1D velocity model is then used as the starting model for the 3D tomographic inversion. The process for 3D inversion is similar to the 1D inversion steps except that "model smoothing – 3D Smooth Velocity" is done to smooth both the Vp and Vs distributions to eliminate areas in the velocity grid with high velocity perturbations. This smoothed model is then used as the next starting modeling and the process continued until stable 3D Vp and Vs models are obtained.

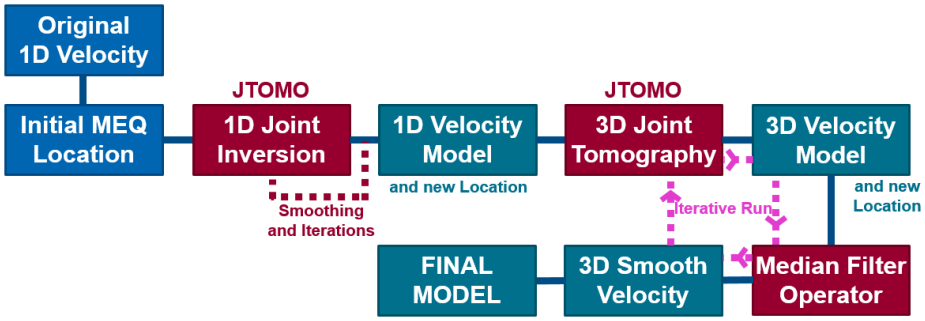

Figure 6: Standard tomography velocity modeling workflow developed by Star Energy Geothermal for developing 1D and 3D velocity models.

For this study, the tomography inversion used MEQ data collected during 2005 to 2018. The dataset available for this period included a total of 13,569 triggers containing 82,416 P-wave and 57,435 S-wave arrival times. This data set was filtered to exclude 'poor quality' events. Table 1 shows the filtering criteria applied for the data used in the inversion.

Table 1. Filtering parameters for events database used during the tomography inversion

No	Filter Parameter	Quantity
1	Minimum Number of Station	5
2	Minimum Number of Picks	6
3	Maximum Error Ellipsoid	500 m
4	Maximum Event Residual	0.25 s
5	Maximum Station GAP	200 deg

These filters resulted in a large reduction of trigger numbers with an output of about 4,000 events (or just ~30% of the initial dataset). Following the workflow described above, the resulting revised 1D model showed slower P-wave velocity for layers below mean sea level (Figure 7), although the trend of velocity change with depth for both models is generally the same. There was a distinct change in the Vp/Vs ratio with the newly developed 1D model having an average Vp/Vs ratio of 1.65, which is lower compared to the original 1D model that has 1.7 Vp/Vs ratio. Geosystem (1998) used Wadati diagram to calculate the Vp/Vs ratio of 230 MEQ events. Considering the significantly larger number of MEQ events used in this recent study, the revised Vp/Vs reflects a better-constrained average due to the better earthquake coverage.

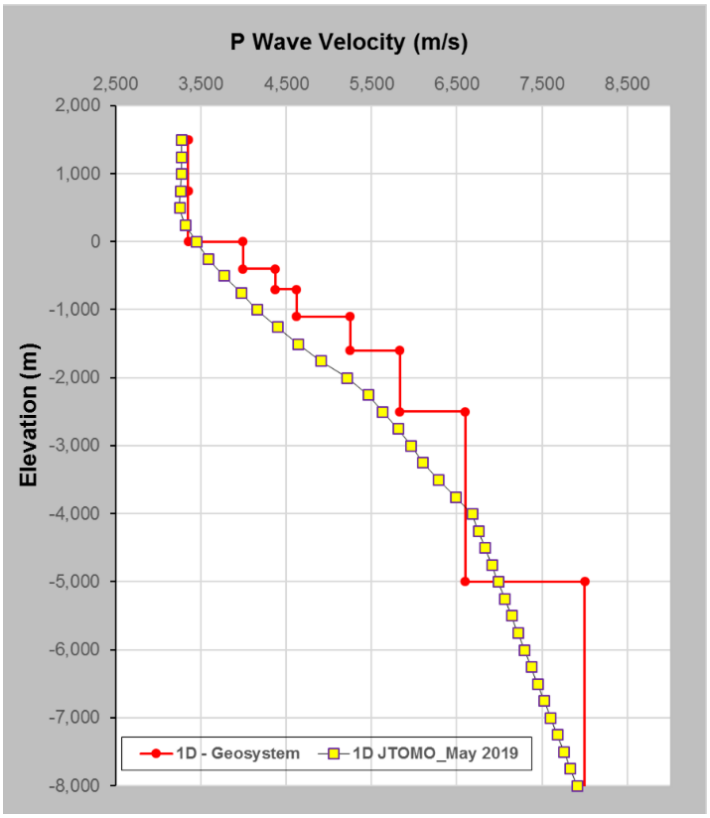

Figure 7: Comparison of the revised 1D tomographic velocity model (2019) and 1D Geosystem model (1998) shows generally the same P-wave velocity change with depth and slower velocity in layers below mean sea level. The 2019 1D model is better constrained than the 1998 1D model considering the significantly larger number of utilized MEQ events used for the tomography inversion.

For the 3D inversion, the model was gridded into cubes of 250 m per side. Station delay calculations were incorporated to solve near-surface velocity uncertainties and station location effects (Nelson, 2018). After the completion of each inversion, new hypocenter locations were determined using the newly inverted velocity model. A quantitative assessment is conducted by analyzing the degree of uncertainty of new MEQ locations. Two of the key uncertainty checks used are the residual mean for the P- and S-phases (modeled vs. observed arrival times) and error ellipsoids. The error ellipsoid calculation uses a Monte-Carlo approach to perturb the travel times based on the residuals for the current location. With the improved data coverage, the revised velocity model should result in improvements and refinements of the velocity model and lower hypocenter uncertainties (Nordquist, 2016). The sequential inversion obviously shows that both the P- and S-phases residuals (observed vs. calculated arrival times) and error ellipsoid are improved. Figure 8 depicts the comparison of error ellipsoid and residual mean of P- and S-phases among the 1998 Geosystem 1D model, 2019 1D model JTOMO, and new 3D model JTOMO.

(a) Error Ellipsoid

Original 1D Model (Geosystem 1998)

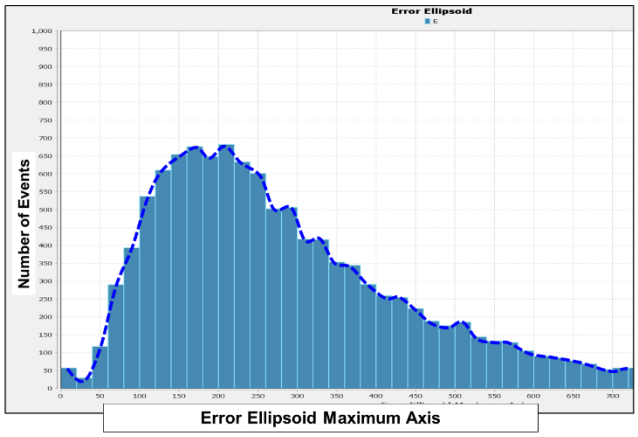

Revised 1D Model JTOMO (2019)

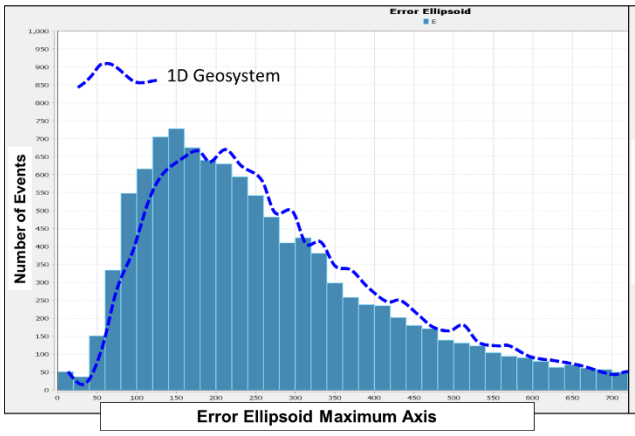

3D Model JTOMO (2019)

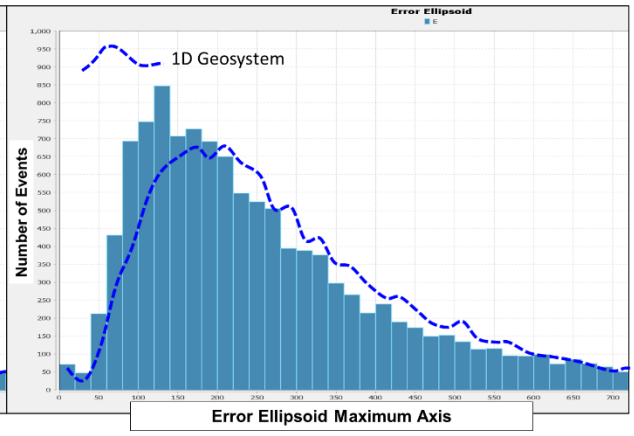

(b) P and S Phases Residual Mean

Original 1D Model (Geosystem 1998)

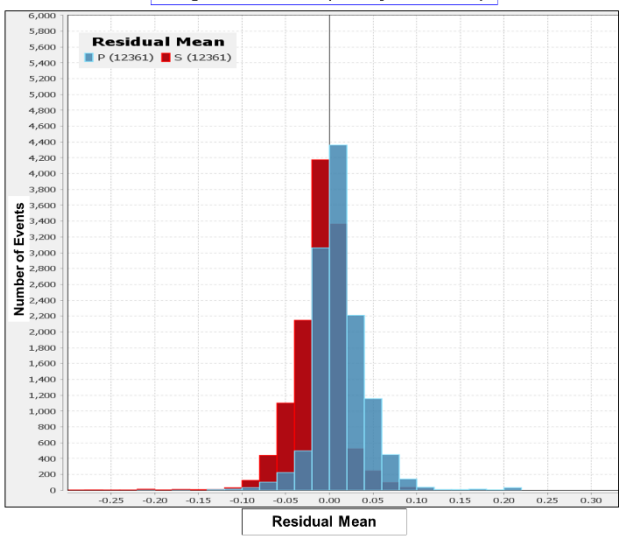

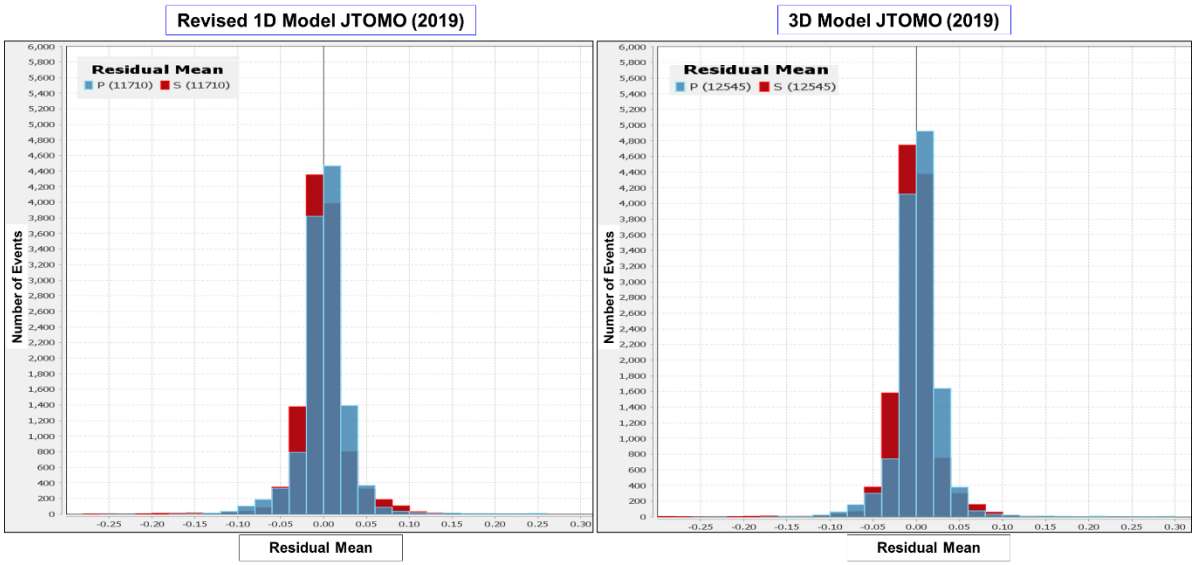

Figure 8: Degree of uncertainty comparison of hypocenter locations based on the 1998 1D model, 2019 1D JTOMO model, and new 3D JTOMO model. The top row histograms (8a) show the reduction of error ellipsoid after relocating from the MEQs using the 1998 ID model, 2019 1D JTOMO and new 3D JTOMO. The bottom histograms (8b) show improvement of P- and S-phases residual mean from the same three models.

A check of the residual mean and error ellipsoids indicates distinct improvements for the 2019 1D and 3D velocity models. Comparison of the error ellipsoids of the 1998 Geosystem 1D model shows that the 2019 1D JTOMO and new 3D JTOMO models are more skewed to the left indicating general error reductions compared to the 1998 1D model (Figure 8a). In addition, the residual mean of P- and S-phases for both the 2019 1D and 3D JTOMO models, show distinctly tighter clustering and the improved and regular distribution about zero (Figure 8b).

4. RESULTS AND DISCUSSION

MEQ epicenter and hypocenter locations based on the new 3D velocity model tend to cluster more tightly and show deeper vertical extension of the MEQ clusters (up to about 500 m) in the eastern part of the field. The new 1D and 3D JTOMO models define systematic lateral and vertical changes of the Salak geothermal reservoir's Vp and Vs velocity structures, including lower Vp centered over the productive field. Cross-plots of Vp with pressure and matrix porosity suggest these parameters may play a role in the reservoir's Vp distribution across the field. These preliminary observations play a role in the integration of these new results into the Static Earth Model in interpreting the base of connected fractures, which translates to the Base of Reservoir (BoR).

4.1 MEQ Event Relocations

The 1998 1D and 2019 3D velocity models do not show significant differences in the MEQ epicenters. Figure 9 shows epicenter maps from both the 1998 1D and 2019 3D models for West Salak. In this portion of the field, the majority of MEQs have been strongly associated with injection activity. In the western field margin, dense clusters of MEQ are associated with brine injection in Awi 9 and condensate injection in Awi 12 and Awi 20. There are also large distinct clusters related to condensate injection in Awi 18 wells farther west and outside of the commercial reservoir. The Awi 18 injectors were drilled in the Cianten Caldera area and were interpreted to have intercepted a fracture system that is not (or very poorly) connected to the productive Awibengkok reservoir. Currently, the Awi 18 wells are utilized as condensate injectors for power plant Units 1-3.

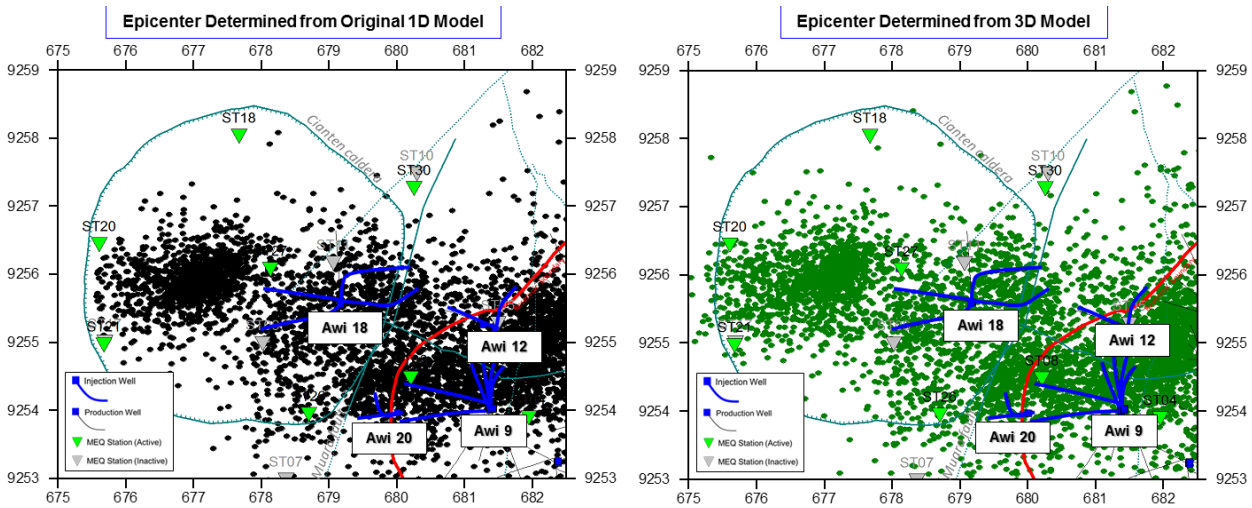

Figure 9: MEQ epicenter maps using the 1998 1D and 2019 3D velocity models. MEQ clusters in West Salak show similar distributions for both the 1D and 3D locations.

To provide a more robust and quantitative analysis, a calculation of epicenter locations difference between the 1998 1D and 2019 3D locations was conducted. The calculation was conducted by subtracting the 3D easting (X-axis) and northing (Y-axis) locations from the 1D locations. Table 2 confirms that the average differences of both locations are very small. The shift in the easting direction has median and mean values of 21 m and -1 m, respectively. For the northing shift, median and mean values are 3 m and 1 m, respectively.

Table 2. Comparison of the difference of MEQ epicenter locations for the 2019 3D model compared to the 1998 1D Geosystem model.

	Easting (X)	Northing (Y)
Median	21 meters	3 meters
Mean	-1 meter	1 meter
Standard Dev.	160 meters	106 meters

Notes:
Positive (+) Easting means shift to East, and vice versa
Positive (+) Northing means shift to North, and vice versa

The distribution of epicenter shift calculation is shown in Figure 10. Although there are a number of events that have larger shift, the majority of shifted epicenter are only about 25 to 50 m for both the X- and Y-directions.

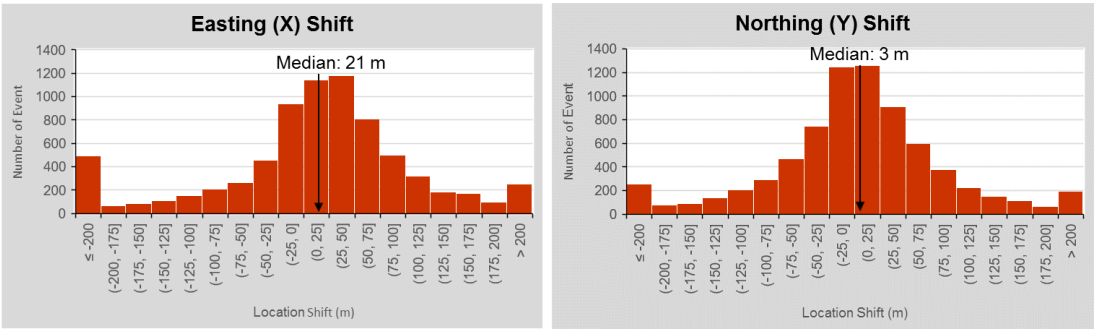

Figure 10: Histograms of the shift calculation of epicenter between the 1D and 3D locations are very small.

Unlike the MEQ event epicenters, there is a distinct hypocenter result between original 1D locations and 3D locations. Distribution of event hypocenters show that in general, MEQ events from the new 3D velocity model result in deeper depth compared to their previous locations. There has been an obvious tightening of MEQ clusters in the central part and general shift-down of MEQ hypocenters in Salak fieldwide. This generally deeper MEQ events distribution is understandable since the new inversion result showed lower Vp/Vs ratio with an average of 1.65. This compared to the Geosystem 1D model that used 1.7 Vp/Vs ratio. This difference in the Vp/Vs ratio as would be expected has impact to the hypocenter locations of the events.

Figure 11 shows a comparison of MEQ occurrence associated with the southern injectors (i.e., Awi 22 and 15) and central production wells using the 1998 1D and 2019 3D models. The new MEQ hypocenter locations show a more reasonable distribution in that MEQs occur inside the geothermal reservoir. The deep MEQs in the south related to injection at Awi 15 and Awi 22 suggest that the injectate reach a deeper fracture system. The MEQ clusters in the south is shifted about -500 m deeper from the prior locations using the 1998 1D model. In addition, the central MEQ clusters related to production activity defined from the 3D model are more tightly grouped and concentrated in the depth range of production feed zones below the Top of Reservoir (ToR). The new MEQ hypocenters from the 2019 3D model removed the shallow MEQs above the interpreted ToR.

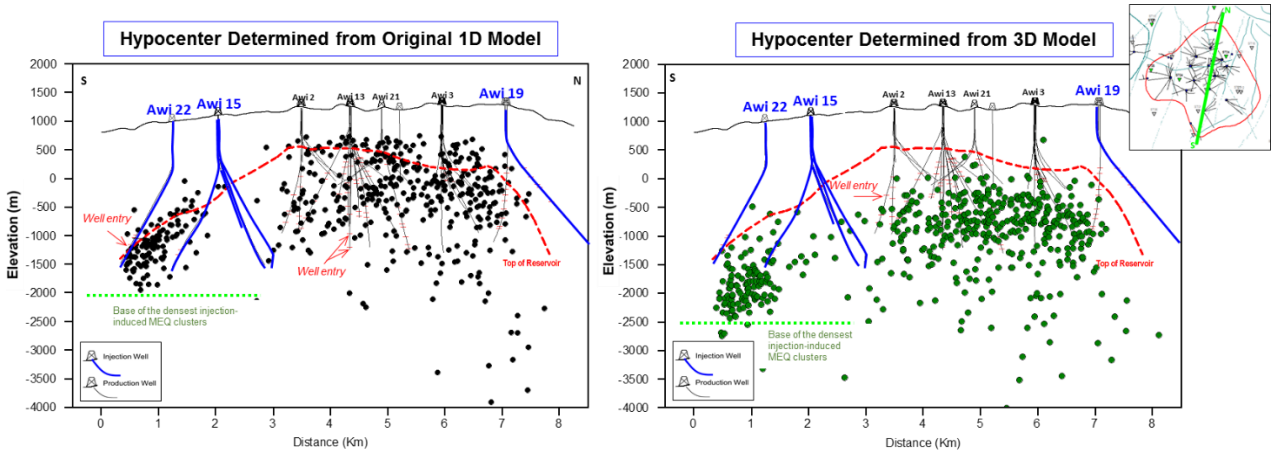

Figure 11: S-N cross-sections showing the distribution of MEQ hypocenters from original 1998 1D velocity model (left) and 2019 new 3D model (right). Fieldwide, MEQ hypocenters are shifted deeper and more tightly grouped in the central production area.

While the MEQ hypocenters shown in Figure 11 exhibit a general deepening using the 2019 3D model, this is not the case for the MEQs related to injection at Awi 9 (Figure 12). Although the base of the densest MEQ clusters has similar depths of about 3,500 m BSL for both the 1998 1D and 2019 3D velocity model locations, MEQs in the central and eastern portions of the field tend to be deeper using the 2019 3D model. Similar with Figure 11, most of the MEQs shown in Figure 12 occur below the ToR.

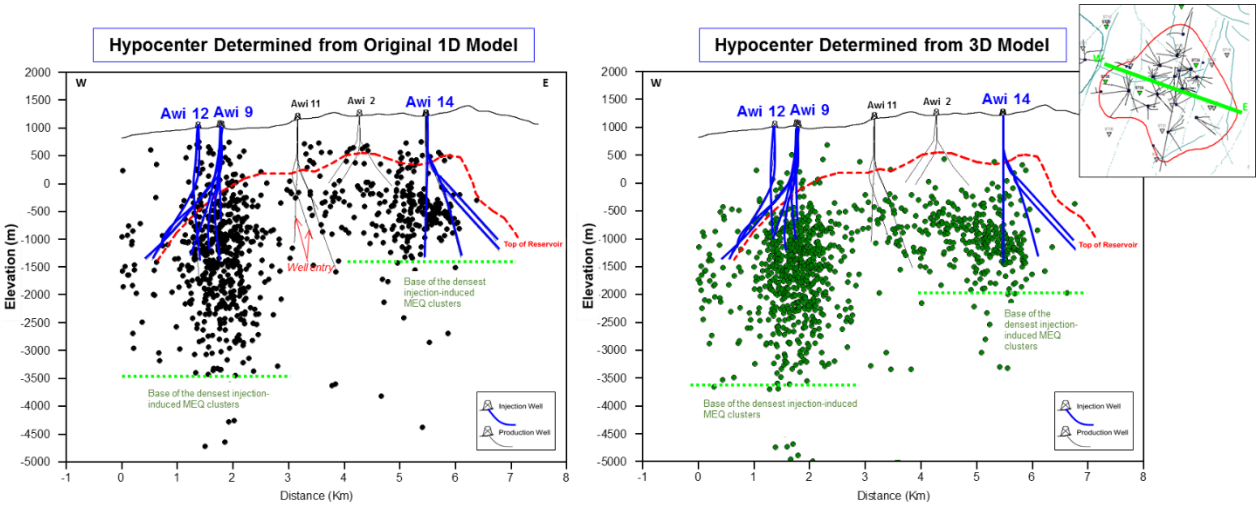

Figure 12: W-E cross-sections showing the distribution of MEQ hypocenters from the original 1998 1D velocity model (left) and hypocenters from new 2019 3D model (right). In the western portion of the field, MEQ hypocenters show similar depths using both models. In the central and eastern part of the field, MEQs using the 3D model are consistently deeper by an average of 500 m.

4.2 Base of Reservoir Definition

The new MEQ hypocenter locations impact the interpreted Base of Reservoir (BoR) in the Static Earth Model. The definition of BoR surface is critical in calculating the size of the general reservoir container in the Static Modeling Workflow (Lubis, 2018). In Salak, the BoR consists of two definitions: base of commercial reservoir and base of connected fracture network in the reservoir. The base of commercial reservoir is determined by the distribution of the deepest feed zone encountered by the deepest well in each well pad. The base of connected reservoir is interpreted from the distribution and depth of the MEQ clusters related to the injectors. It is believed that these injection-related MEQ clusters are imaging the vertical extent of the stimulated/connected fracture network.

The workflow for the interpretation of the BoR uses the MEQ event densities that are computed in the Static Earth Model and gridded. The previous BoR surface was updated in 2016 and used the MEQ locations based on the original 1998 1D velocity model. The new and deeper hypocenters in several portions of the field resulting from the 2019 3D model, especially the central and eastern field, has led to a revision in the interpretation of the BoR (Figure 13). This revised interpretation is integrated into the Static Earth Model and is being used to update the Dynamic Model or Numerical Simulator.

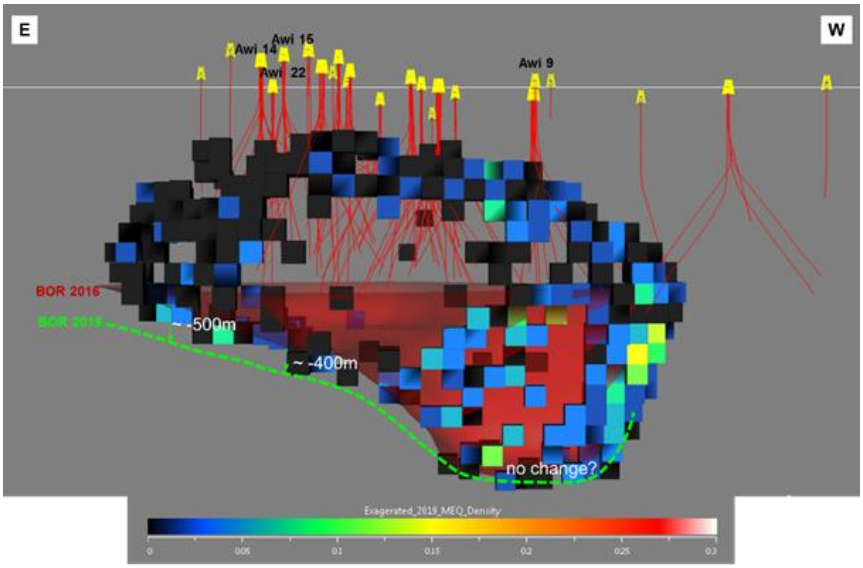

Figure 13: Using the deeper MEQ hypocenters from the 2019 3D velocity model, the Salak BoR was slightly adjusted, by as much as 500 m in certain areas of the reservoir (view from north).

4.3 Velocity Structure

The resulting velocity structure from the 3D tomographic modeling delineates a distinct variation of velocity signatures within the Salak geothermal reservoir. Interestingly, lower Vp velocities are shown within the production area (Figure 14). The strongest low Vp anomaly concentrated in the area near Awi 7, Awi 8, and Awi 21 production wells. A small area of slightly higher velocity is observed near Awi 2 and Awi 13 wells in the mid-to-south production area and northern-most parts of the reservoir (Figure 14).

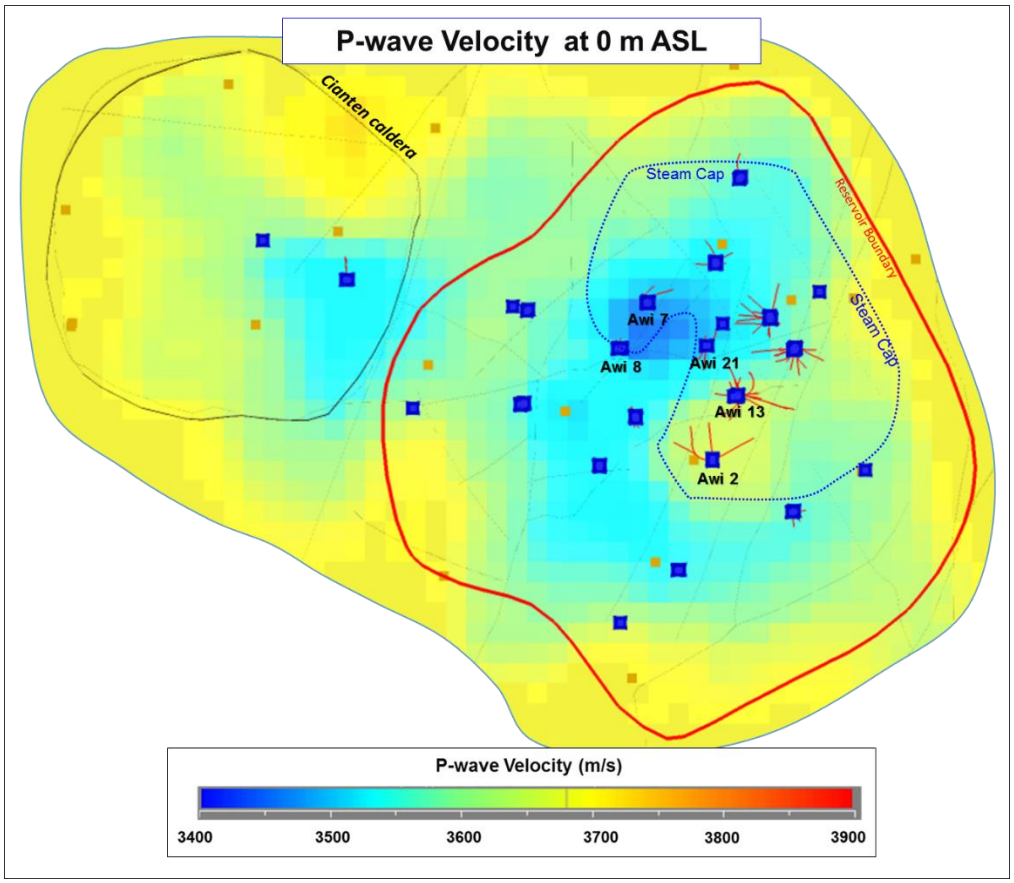

Figure 14: P-wave velocity (Vp) structure at mean sea level. Majority of the production area has low Vp, which extends to the west in Awi 18. A small, distinct higher Vp area appears near Awi 2 and Awi 13.

The area with lower Vp corresponds to the area with lower reservoir pressure. Figure 15 shows the distribution of reservoir pressure in 2005 and 2016 at ~30 m ASL. The difference in pressure distribution between 2005 and 2016 reflects the pressure drop in the reservoir because of mass extraction. The largest pressure drop is located in the central production area. Meanwhile, the area in the vicinity of Awi 9 shows slower rates of pressure decrease. These features coincide pretty well with the distributions of Vp. The link between the Vp and reservoir pressure is also supported by the correlation of both parameters shown in the cross-plot in Figure 16. In addition, cross-plots of Vp with other reservoir properties, e.g., matrix porosity, fracture permeability, and temperature, indicates that the velocity has good correlation with matrix porosity and fracture permeability but is less correlatable with temperature (Figure 17; Mendrofa, 2018).

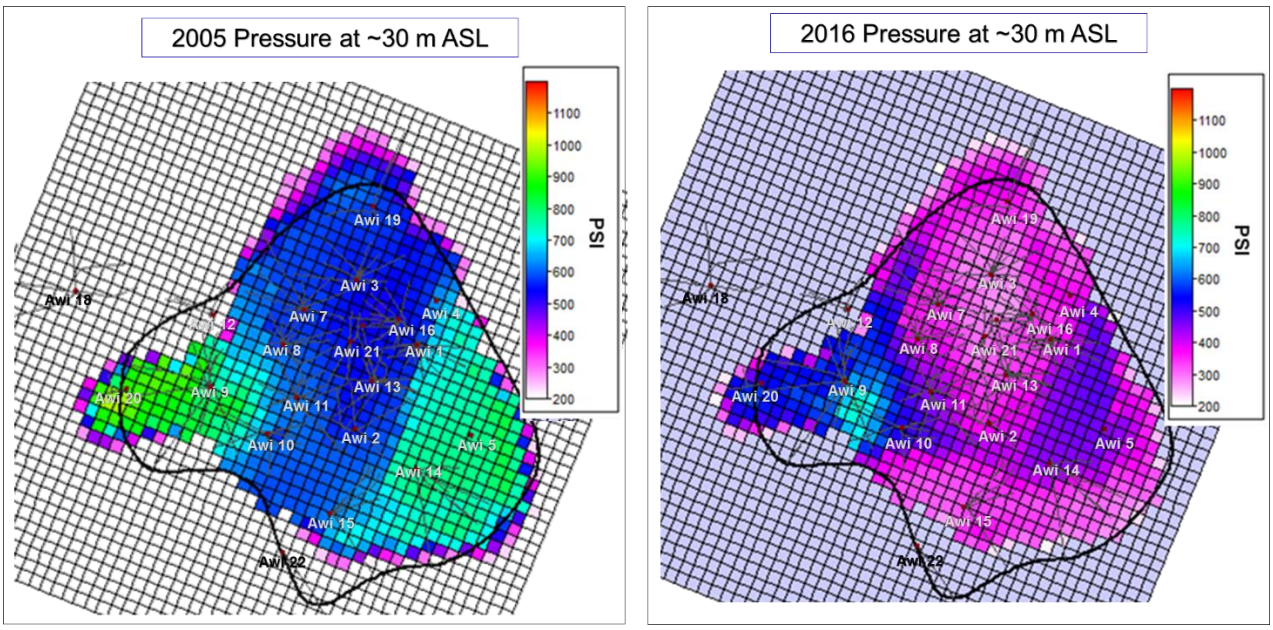

Figure 15: Map showing the distribution of reservoir pressure at about 30 m ASL in 2005 (left) and 2016 (right). Both figures indicate that the central production has experienced larger pressure drop in Salak Field.

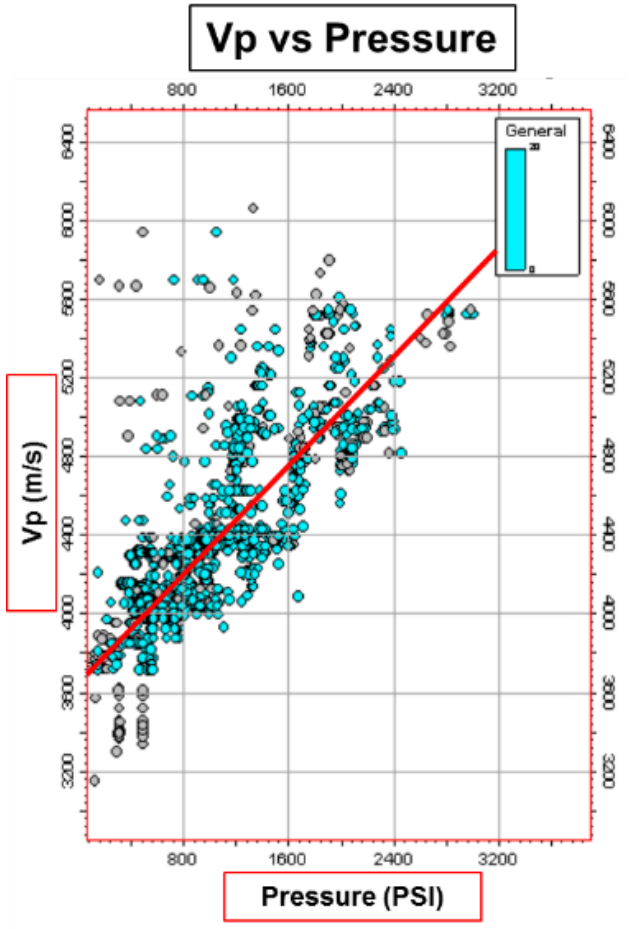

Figure 16: Cross-plot of Vp and reservoir pressure shows their positive correlation and supports the concurrence of the distribution of low Vp and pressure drop in the reservoir.

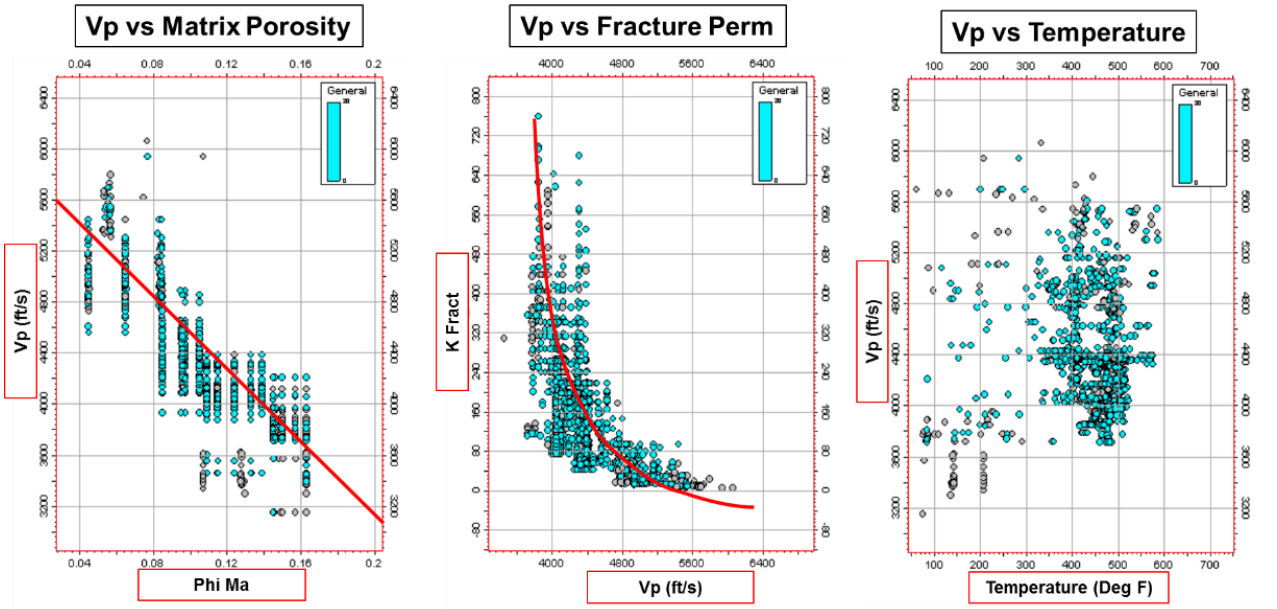

Figure 17: Cross-plots of Vp with matrix porosity, fracture permeability, and temperature indicate that Vp has good correlations with matrix porosity and fracture permeability, but is less correlatable with temperature.

The relatively higher anomaly of Vp at mean sea level (Figure 14) near Awi 2 and Awi 13 producers coincides with the area that has experienced the highest land subsidence at Salak field (Figure 18). Higher Vp anomaly continued to appear at depth of 250 m BSL. Maximum subsidence during elevation monitoring in 1998 to 2017 is about -56 cm. Subsidence is related to mass extraction and resulting pore compaction. The concurrence of locations of high Vp and large land subsidence area suggests that subsidence occurrence in Salak could be the cause of the relatively high Vp velocity signatures in this part of the reservoir.

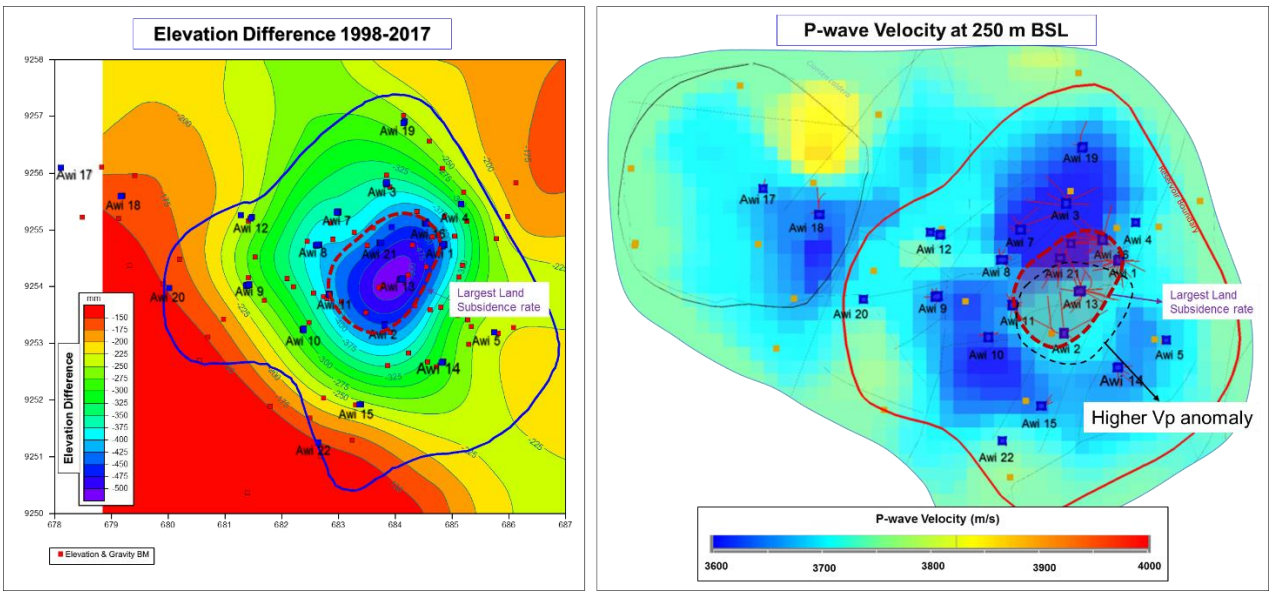

Figure 18: Map of Salak land subsidence occurrence and Vp distribution at 250 m BSL. The largest land subsidence has coincident location with the higher anomaly of Vp in the central part of the field.

5.CONCLUSIONS

The utilization of the Microseisgram/JTOMO (Altcom, Ltd.) application for tomography velocity modeling provided new insight to further characterize the Salak geothermal reservoir. The new 3D tomographic velocity model resulted in lower uncertainty for locations of the MEQ. This results in higher level of confidence on microseismicity interpretation and the integrated understanding of reservoir fracture network including interpretation of the BoR. The velocity structure showed distinct vertical and lateral changes and exhibited good correlation with several reservoir properties, including reservoir pressure, matrix porosity, and fracture permeability. Further analysis will be conducted by applying time-lapse tomography to have better understanding of the link between velocity and petrophysical properties. A conclusive resolution of Vp and petrophysical properties linkage is expected to assist improve the Static Modeling Workflow.

Other microseismic analysis such as double difference, focal mechanism study, and shear-wave splitting are being tested by SEG. Preliminary results from these studies seem to be encouraging, as workflows were developed and tested for application on SEG's extensive MEQ databases. It is expected that application of these techniques could provide insight for reservoir characterization.

REFERENCES

Acuna, J.A., Stimac, J.A., Sirad-Azwar, L., Pasikki, G.R.: Reservoir Management at Awibengkok Geothermal Field, West Java, Indonesia, *Geothermics*, **37**, (2008), 332–346.

Biasi, G., et al.: Body Wave Tomography for Regional Scale Assessment of Geothermal Indicators in the Western Great Basin, *GRC Transactions*, **33**, (2009).

Geosystem srl.: Analysis of Microearthquake Data, Awibengkok Geothermal Field, West Java, Republic of Indonesia, Unpublished report prepared for Unocal Geothermal Indonesia (1998).

Gibson, G., and Sandiford, M.: Seismicity and Induced Earthquakes, Melbourne Energy Institute, University of Melbourne, a background paper to the office of the NSW Chief Scientist and Engineer (OCSE) (2013).

Kissling, E., Ellsworth, W.L., Eberhart-Phillips, D., and Kradolfer, U.: Initial Reference Models in Local Earthquake Tomography, *Journal of Geophysical Research*, **99**, (1994), 19,635–19,646.

Lubis, T., and Perdana, M.W.: 2018 Salak Base of Reservoir Surface Memorandum, Unpublished Star Energy Geothermal Salak Internal Memorandum (2018).

Mossop, A., and Segall, P.: Unpublished work on mechanisms of Geysers injection-induced seismicity: Correlations and Interpretations, available at Department of Geophysics, Stanford University (2004).

Mendrofa, D.: Analysis on Vp-Vs Links to Petrophysical Parameters, Unpublished Star Energy Geothermal Salak Internal Document (2018).

Nelson, C., Widodo, A., and Kusmayadi, H.: Salak Annual Microseismic Report 2011, Unpublished Chevron Internal Memorandum (2012).

Nelson, C., Nordquist, G., Tanuwidjaja, R., Jupe, A.: Injection-induced Microearthquakes for Reservoir Characterization in Darajat Geothermal Field, Indonesia, *GRC Transactions*, **42**, (2018).

Nordquist, G.: Darajat - Updated Velocity Model and Next Steps– First Application MicroSeisGram/JTOMO, Unpublished Chevron Internal Memorandum (2016).

Nordquist, G., Suminar, A., Sugiaman, F., and Azof, I.: Awibengkok Microearthquakes – Analysis and Interpretation Update, Unpublished Unocal Internal Report (1998).

Paige, C., and Saunders, M.: LSQR: Sparse Linear Equations and Least Squares Problems, *ACM Trans. Math. Softw. 8, 2,* (1982), 195–209.

Perdana, M.W.: 2018 Salak Tomography Velocity Modeling, Unpublished Star Energy Geothermal Salak Internal Memorandum (2018).

Perdana, M.W., Widodo, A., and Kusmayadi, H.: Salak Annual Microseismic Report 2017, Unpublished Star Energy Geothermal Salak Internal Memorandum (2018).

Stimac, J., Nordquist, G., Suminar, A., and Sirad-Azwar, L.: An overview of the Awibengkok geothermal system, Indonesia, *Geothermics*, **37**, (2008), 300–331.

Soeparjadi, R., Horton, G.D., and Wendt, B.E.: A review of the Gunung Salak Geothermal Expansion Project, *Proceedings*, 20th New Zealand Geothermal Workshop, Auckland, pp. 153–158 (1998).

Tanuwidjaja, R., Nelson, C., Nordquist, G.: Injection Induced Seismicity at Western Salak Geothermal Field, *Proceedings*, Indonesia International Geothermal Convention and Exhibition 2015, Jakarta, Indonesia (2015).

Wibowo, D.A.S., Nordquist, G., Stimac, J., and Suminar, A.: Monitoring Microseismicity during Well Stimulation at the Salak Geothermal Field, Indonesia, *Proceedings*, World Geothermal Congress 2010, Bali, Indonesia (2010).